



Dalton  
Transactions

**Materials design, synthesis, and transport properties of  
disordered rare-earth Zintl bismuthides with the anti-Th3P4  
structure type**

Journal:	<i>Dalton Transactions</i>
Manuscript ID	DT-ART-02-2022-000412.R1
Article Type:	Paper
Date Submitted by the Author:	01-Mar-2022
Complete List of Authors:	Ogunbunmi, Michael; University of Delaware, Chemistry and Biochemistry Baranets, Sviatoslav; University of Delaware, Chemistry and Biochemistry Bobev, Svilen; University of Delaware, Chemistry and Biochemistry

SCHOLARONE™  
Manuscripts

## ARTICLE

# Materials design, synthesis, and transport properties of disordered rare-earth Zintl bismuthides with the *anti*-Th<sub>3</sub>P<sub>4</sub> structure type

Received 00th January 20xx,  
Accepted 00th January 20xx

DOI: 10.1039/x0xx00000x

Michael O. Ogunbunmi,<sup>a</sup> Sviatoslav Baranets,<sup>a</sup> Svilen Bobev<sup>a,\*</sup>

The synthesis, structural elucidation, and transport properties of the extended series Ca<sub>4-x</sub>RE<sub>x</sub>Bi<sub>3</sub> (RE = Y, La–Nd, Sm, Gd–Tm, Lu; x ≈ 1) and Ca<sub>4-x</sub>RE<sub>x</sub>Bi<sub>3-δ</sub>Sb<sub>δ</sub> (RE = La, Ho, Er, Lu; x ≈ 1, δ ≈ 1.5) are presented. The structural elucidation is based on single-crystal X-ray diffraction data and confirms the chemical drive of Ca<sub>4</sub>Bi<sub>3</sub> with the cubic *anti*-Th<sub>3</sub>P<sub>4</sub> structure type (space group *I* $\bar{4}3d$ , no. 220, Z = 4) into a Zintl phase by the introduction of trivalent rare-earth atoms. The structure features complex bonding, heavy elements, electron count akin to that of the valence-precise semiconductors, making it an ideal target for thermoelectrics development. Introducing crystallographic site disorder at the cation site for Ca<sub>4-x</sub>RE<sub>x</sub>Bi<sub>3</sub> and on both cation and anion sites for Ca<sub>4-x</sub>RE<sub>x</sub>Bi<sub>3-δ</sub>Sb<sub>δ</sub> phases bring about additional desirable characteristics for thermoelectric materials in the context of tuning knobs for lowering the thermal conductivity. Electronic structure calculations on idealized Ca<sub>3</sub>YBi<sub>3</sub> and Ca<sub>3</sub>LaBi<sub>3</sub> compounds indicate the opening of indirect bandgaps at the Fermi level with magnitudes  $E_g = 0.38$  eV and 0.57 eV, respectively. The electrical resistivity  $\rho(T)$  of some of the investigated phases measured on single crystals evolve in a metallic manner with magnitudes of the order of 1.4 m $\Omega$ .cm near 500 K, thus supporting the notion of a degenerate semiconducting state, with temperature dependence of the Seebeck coefficient  $\alpha(T)$  suggesting *p*-type behavior. The low electrical resistivity and the realization of a degenerate semiconducting state in the title phases present a window of opportunity for optimizing their carrier concentration for enhanced thermoelectric performance.

## Introduction

Zintl phases are compounds of metals that are often characterized by semiconducting behaviors. They present a fertile playground to explore the various electronic and transport properties of materials of interests ranging from the topological phases of matter<sup>1,2</sup> to applications in thermoelectrics<sup>3</sup> and photovoltaics<sup>4,5</sup>. Leveraging on the idea of the Zintl-Klemm concept<sup>6</sup> thus allows for a myriad of opportunities to both conceptualize, design, and grow new materials at the heart of cutting-edge technological applications. More intuitively, the Zintl-Klemm concept allows for exploring the various structure-property relationships and the subsequent optimization of such properties from the understanding of the electron counts and bonding.

Structural complexity that has to do with intricate chemical bonding is another hallmark of the Zintl phases; this can give

rise to glass-like thermal conductivity and a high electrical conductivity driven by their narrow bandgap<sup>2,3,7</sup>. As such, materials that combine these features with a significantly high Seebeck coefficient are of interest in achieving an enhanced thermoelectric figure of merit  $zT = \alpha^2\sigma/(\kappa_e + \kappa_l)$  at a given operating temperature  $T$ . Here,  $\alpha$ ,  $\sigma$ ,  $\kappa_e$  and  $\kappa_l$  are the Seebeck coefficient, electrical conductivity, electronic thermal conductivity, and lattice thermal conductivity, respectively<sup>7</sup>.

The incorporation of magnetic species into a crystal structure that can birth an intrinsic magnetic phase transition as well as the manifestation of heavy-fermion state<sup>8–10</sup> are now being explored as new routes to enhanced thermoelectric performance. Furthermore, the interest in magnetic topological insulators has been on the rise recently owing to the plethora of exotic states of matter that may be observed in such materials. As such, Zintl phases that combine ions with localized unpaired electrons with excellent thermoelectric properties are likely candidates to explore for such exotic states of matter<sup>2,11,12</sup>. This is simply because several emergent thermoelectric materials are also known to host topological properties<sup>13</sup>.

Substitution studies aimed to achieve a balanced electron count and with an attendant crystallographic disorder are fueled by the desire to achieve an optimal performing thermoelectric generator. One of such studies carried out is

<sup>a</sup> Department of Chemistry and Biochemistry, University of Delaware, Newark, Delaware, 19716, United States.

\* Corresponding author Email: [bobev@udel.edu](mailto:bobev@udel.edu).

Electronic Supplementary Information (ESI) available: tables with crystallographic data for all refined structures; results from the electronic structure calculations for Ca<sub>4</sub>Bi<sub>3</sub>; details from additional calorimetry and electron microscopy work. See DOI: 10.1039/x0xx00000x

$\text{Yb}_{4-x}\text{RE}_x\text{Sb}_3$  ( $\text{RE} = \text{La}, \text{Sm}$ )<sup>14,15</sup> and the recently reported  $\text{Ca}_{4-x}\text{RE}_x\text{Sb}_3$  ( $\text{RE} = \text{La-Nd}, \text{Sm}, \text{Gd-Tm}, \text{Lu}$ ) phases<sup>16</sup>, denoted hereafter as  $\text{Ca}_3\text{RESb}_3$ . The results in these studies clearly demonstrate the role-play of the trivalent  $\text{RE}$  atoms substitution on the cubic  $\text{RE}_4\text{Sb}_3$ <sup>17-19</sup> phases with the *anti*- $\text{Th}_3\text{P}_4$  structure type in achieving a narrow bandgap semiconducting state due to the closed-shell electronic configuration achieved by all the elements. From the structure-property point of view, this happens to be yet another effort in enhancing the thermoelectric properties and thus highlights these materials as promising candidates to further explore the techniques of band engineering and carrier concentration tuning for enhanced thermoelectric performance.

Going forward, one might wonder what the picture would look like if the  $\text{Sb}$  atoms were to be isovalently replaced by  $\text{Bi}$  atoms, which are much heavier. What would be the impact of such substitution on the electrical conductivity and thermal conductivity? How does the metallic nature of  $\text{Bi}$  affect the size of the bandgap? How does the carrier concentration respond to the new material modification and the resultant effect on the magnitude of the Seebeck coefficient? All these are open questions that beckon for answers. In addition, it is even possible to further introduce another site disorder in the crystal structure by splitting the  $12a$  unique position (see crystal structure description *vide infra*) between  $\text{Sb}$  and  $\text{Bi}$  atoms and see how these imparts on the transport properties. Thus, this work builds on the strength of previous works and explores this line of thought to answer some of the open questions. Since the syntheses of new materials are vital to solid-state research endeavors and at the heart of promising technological applications, we provide another exciting twist to the substitution studies on the cubic  $\text{RE}_4\text{Sb}_3$ <sup>17-19</sup> phases. We present our results on the synthesis, crystal structure as well as electronic and transport properties of thirteen new solid solutions  $\text{Ca}_{4-x}\text{RE}_x\text{Bi}_3$  ( $\text{RE} = \text{Y}, \text{La-Nd}, \text{Sm}, \text{Gd-Tm}, \text{Lu}; x \approx 1$ ), as well as four members of the  $\text{Ca}_{4-x}\text{RE}_x\text{Bi}_{3-\delta}\text{Sb}_\delta$  ( $\text{RE} = \text{La}, \text{Ho}, \text{Er}, \text{Lu}, x \approx 1$ ) family, and provide an intuitive understanding to their thermoelectric properties. For brevity, the title compounds will be referred to as  $\text{Ca}_3\text{REBi}_3$  and  $\text{Ca}_3\text{REBi}_{3-\delta}\text{Sb}_\delta$  hereafter.

## Experimental

### Synthetic procedures

Single crystals of  $\text{Ca}_3\text{REBi}_3$  ( $\text{RE} = \text{Y}, \text{La-Nd}, \text{Sm}, \text{Gd-Tm}, \text{Lu}$ ) were grown via the flux method using molten  $\text{Pb}$ . The synthesis procedure involves weighing starting elements  $\text{Ca}:\text{RE}:\text{Bi}:\text{Pb}$  in the 3:1:3.2:25 ratio inside an  $\text{Ar}$ -filled glovebox. The elements were used as purchased from Sigma-Aldrich and Alfa-Aesar with typical purity of  $\geq 99.9$  wt.%. The weighed elements were loaded into alumina crucibles and encased in fused silica ampoules packed between two balls of quartz

wool. The ampoules were subsequently evacuated and flame-sealed under a vacuum. They were then loaded into a muffle furnace in an upright manner, heated to 1323 K at the rate of 100 K  $\text{h}^{-1}$ , and homogenized at this temperature for 24 h. The reaction was then slowly cooled to 873 K at the rate of 3 K  $\text{h}^{-1}$  after which the fused-silica tubes were quickly removed from the furnace, flipped, and spun in a centrifuge at high speed to remove excess molten  $\text{Pb}$ . The tubes were then taken to the  $\text{Ar}$ -filled glove box, opened, and the synthesized product(s) were extracted. Millimeter-sized crystals were obtained from most reactions involving the light rare-earth elements ( $\text{RE} = \text{La-Nd}, \text{Sm}$ ) while for the heavy rare-earth elements, the obtained crystals were noticeably smaller. In addition, while the reactions with the light rare-earth elements mainly contain the desired phase, those with the heavy rare-earth elements were found to be yielding multiphase products—crystal of micron sizes of the desired phase, along with similar in appearance but typically much larger crystals isotopic with the  $\text{Ca}_{11}\text{Bi}_{10}$  binary phase<sup>20</sup>. Importantly,  $\text{Pb}$ -flux reactions with the  $\text{Ca}:\text{RE}:\text{Bi}:\text{Pb}$  ratio 3:1:3.2:25 ( $\text{RE} = \text{Tm}, \text{Lu}$ ) also afforded very large  $\text{Ca}_{14-x}\text{RE}_x\text{Al}_{1-y}\text{RE}_y\text{Bi}_{11}$  phases<sup>21</sup>.

Polycrystalline samples of four  $\text{Ca}_3\text{REBi}_{3-\delta}\text{Sb}_\delta$  ( $\delta \approx 1.5$ ) were prepared using the direct reaction route. The synthesis procedures involve weighing the elements  $\text{Ca}:\text{RE}:\text{Bi}:\text{Sb}$  in the 3:1:1.5:1.5 ratio and loaded into a  $\text{Nb}$ -tube in an  $\text{Ar}$ -filled glovebox. The tube was properly shut and transferred to an arc-welding furnace chamber, which was subsequently evacuated and sealed using  $\text{Ar}$  plasma. The sealed tubes were transferred into a silica tube, evacuated and flame-sealed under vacuum. The as-prepared assemblies were then placed in tube furnaces and heated to 1298 K at the rate of 100 K  $\text{h}^{-1}$  and maintained at this temperature for 72 h before being quenched in cold water. The silica tubes were opened, and the  $\text{Nb}$ -tubes transferred into a glovebox where they were cut-opened. The products were ground and loaded back into new  $\text{Nb}$ -tubes, then sealed, moved to silica tube, and flame-sealed under vacuum. The samples were then annealed at 1298 K for 10 days before quenching in cold water. The phase identification of the products reveals the  $\text{Ca}_3\text{REBi}_{1.5}\text{Sb}_{1.5}$  compounds with minute amounts of  $\text{RESb}/\text{Bi}$  impurities. For the densification of the samples for transport measurements, a few portions of the prepared  $\text{Ca}_3\text{REBi}_{1.5}\text{Sb}_{1.5}$  samples were finely grounded using an agate mortar and pestle and transferred into a 5 mm diameter die, and a pressure of 2 tons was applied for about 2 minutes. The respective pellets were then transferred into an alumina crucible lined with  $\text{Mo}$  sheet, placed in a quartz tube, and flame sealed under vacuum. The ampoules were then rapidly heated to 600 K over an hour, kept at this temperature for another hour, and then quenched in cold water. The percentage of the density observed as compared to the theoretically calculated values is  $\sim 86\%$ . In Figure 1, the SEM images of single crystal of  $\text{Ca}_3\text{LaBi}_3$  and polycrystalline  $\text{Ca}_3\text{HoBi}_{1.5}\text{Sb}_{1.5}$  are shown, respectively.

## ARTICLE

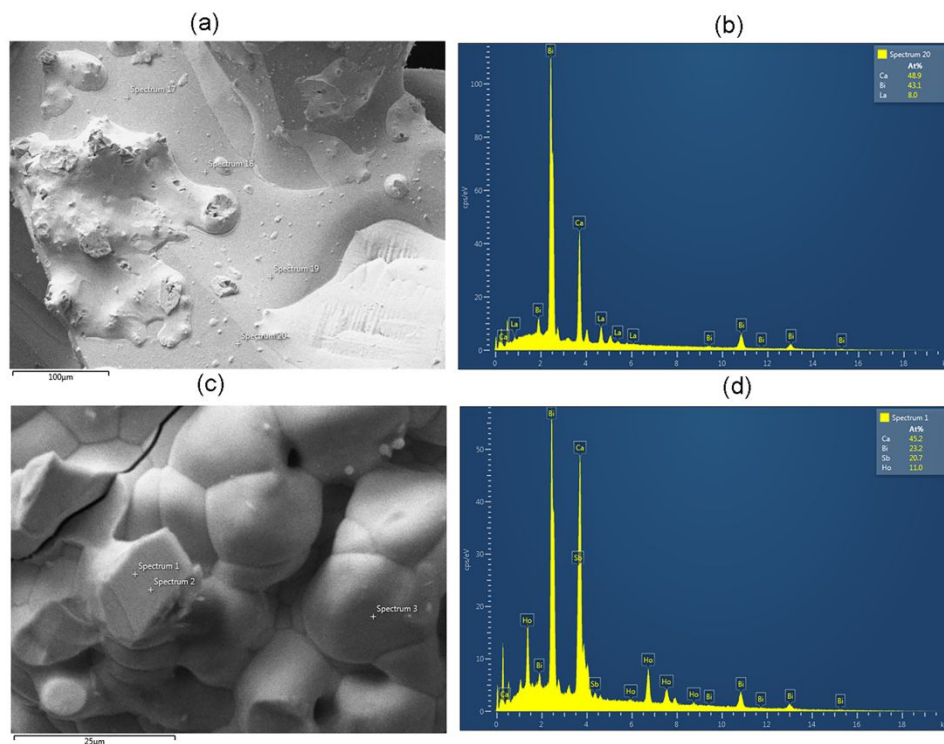


**Figure 1.** (a) SEM image of single crystal of  $\text{Ca}_3\text{LaBi}_3$  (b) Representative histogram from EDS analysis of  $\text{Ca}_3\text{LaBi}_3$  under high magnification. (c) and (d) SEM image of polycrystalline  $\text{Ca}_3\text{HoBi}_{1.5}\text{Sb}_{1.5}$  and a representative histogram from EDS analysis under high magnification, respectively.

### Crystallography

**Powder X-ray diffraction.** Powder X-ray diffraction (PXRD) measurements were conducted at room temperature on a Rigaku Miniflex diffractometer (filtered  $\text{Cu K}\alpha$  radiation,  $\lambda = 1.5418 \text{ \AA}$ ), operated inside a nitrogen-filled glovebox. Small portions of the obtained single crystals were ground inside an argon-filled glove box using agate mortars and pestles. Data were collected between  $5$  and  $75^\circ$  in  $2\theta$  with a step size of  $0.05^\circ$  and  $2 \text{ s}$  per step counting time. The powder diffraction patterns for the samples were matched with the theoretically generated patterns (based on the crystal structures elucidated based on single-crystal X-ray diffraction methods), which confirmed that the bulk of the phase is the target composition. PXRD measurements before and after exposure to air indicate that the phases are relatively stable in air for up to three weeks. The representative PXRD patterns for  $\text{Ca}_3\text{REBi}_3$  ( $\text{La}$ ,  $\text{Ce}$ ) and  $\text{Ca}_3\text{REBi}_{1.5}\text{Sb}_{1.5}$  ( $\text{RE} = \text{Ho}$ ,  $\text{Er}$ ) phases are presented in Figure 2.

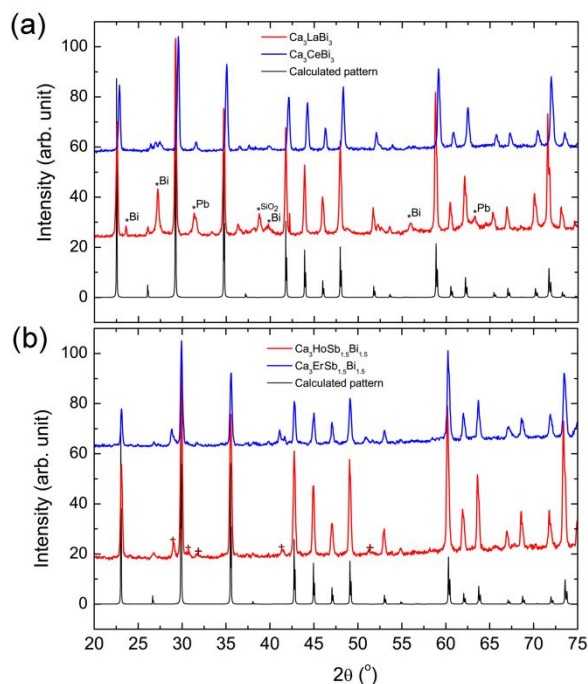


**Figure 2.** (a) Room temperature powder XRD (PXRD) patterns of  $\text{Ca}_3\text{REBi}_3$  ( $\text{RE} = \text{La}, \text{Ce}$ ) – the samples were flux-grown single crystals that were ground to powders, therefore, small peaks from elemental Pb and Bi are also observed. The peak near  $2\theta = 38.5^\circ$  is from quartz. (b) PXRD patterns of polycrystalline  $\text{Ca}_3\text{REBi}_{1.5}\text{Sb}_{1.5}$  ( $\text{RE} = \text{Ho}, \text{Er}$ ) samples. The additional peaks marked with '+' symbols are from minor impurities of binary  $\text{RE}\text{Sb}/\text{Bi}$  phases.

**Single-crystal X-ray diffraction.** Single-crystal X-ray diffraction (SCXRD) studies were performed on a Bruker Photon III diffractometer equipped with a  $\text{Mo } K\alpha$  radiation ( $\lambda = 0.71073 \text{ \AA}$ ) source. Single crystals prepared by flux reactions were immersed in Paratone-N oil and cut into suitable dimensions. The selected single crystal was placed onto a low-background plastic loop holder, quickly moved to the goniometer maintained at 200 K for the whole period of data collection. Measurements were carried out in batch runs with a frame width of  $0.8^\circ$  in  $\omega$  with data collections using a Bruker

software. SADABS software was used for multi-scan absorption correction. Structure solution and refinements were carried out using ShelXT<sup>22</sup> and ShelXL<sup>23</sup> (integrated into Olex2<sup>24</sup> graphical user interface), respectively. STRUCTURE TIDY<sup>25</sup> software was used to standardize the atomic coordinates. In Figure 3, the variation of the unit cell volume across the lanthanide series based on Table 1 is presented.

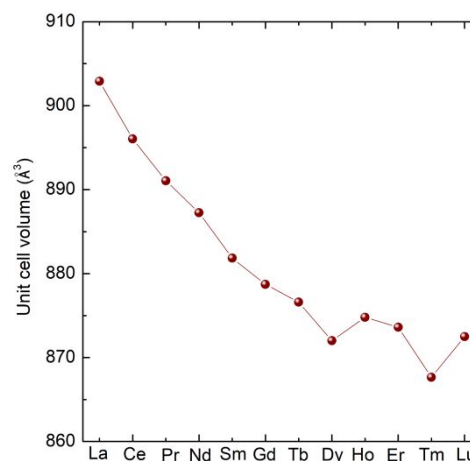


**Figure 3.** Unit cell volumes for the  $\text{Ca}_3\text{REBi}_3$  ( $\text{RE} = \text{Y}, \text{La–Nd}, \text{Sm}, \text{Gd–Tm}, \text{Lu}$ ).

### Elemental analysis

Additional analyses were conducted to verify the elemental composition. Selected single crystals and some polycrystalline samples were mounted on carbon tapes glued to aluminum holders. The analyses were performed on Auriga 60 Cross Beam Scanning Electron Microscope equipped with Oxford Synergy X-MAX80 & EDS (electron backscattering diffraction) X-ray energy-dispersive (EDX) spectrometer. The used beam current was  $10 \mu\text{A}$  at 20 kV accelerating potential. Data were collected over several spots; spectrum maps were taken over the whole samples as well. See Figure 1 for the EDS results, which are consistent with the refined stoichiometry based on SCXRD.

## ARTICLE

**Table 1.** Selected crystallographic data of  $\text{Ca}_3\text{REBi}_3$  ( $\text{RE} = \text{Y, La-Nd, Sm, Gd-Tm, Lu}$ ), measured at 200(2) K, space group  $\bar{1}43d$ ,  $Z = 4$ , Mo  $K\alpha$  radiation  $\lambda = 0.71073 \text{ \AA}$ .

refined formula	$\text{Ca}_{3.29(1)}\text{La}_{0.71}\text{Bi}_3$	$\text{Ca}_{3.33(1)}\text{Ce}_{0.67}\text{Bi}_3$	$\text{Ca}_{3.35(1)}\text{Pr}_{0.66}\text{Bi}_3$	$\text{Ca}_{3.33(1)}\text{Nd}_{0.67}\text{Bi}_3$	$\text{Ca}_{3.23(1)}\text{Sm}_{0.77}\text{Bi}_3$
f.w.	857.43	854.54	853.30	857.05	872.17
$a/\text{\AA}$	9.6653(6)	9.6407(6)	9.6228(5)	9.6091(7)	9.5895(5)
$V/\text{\AA}^3$	902.91(17)	896.04(17)	891.05(14)	887.25(19)	881.84(14)
$\rho_{\text{cal}}/\text{g cm}^{-3}$	6.31	6.34	6.36	6.42	6.57
$\mu/\text{cm}^{-1}$	633.6	639.1	644.2	650.1	665.2
$R_1$ ( $I \geq 2\sigma$ ) <sup>a</sup>	0.0281	0.0202	0.0193	0.0216	0.0182
$wR_2$ ( $I \geq 2\sigma$ ) <sup>a</sup>	0.0615	0.0335	0.0386	0.0326	0.0317
$R_1$ (all data) <sup>a</sup>	0.0308	0.0231	0.0219	0.0253	0.0210
$wR_2$ (all data) <sup>a</sup>	0.0623	0.0345	0.0394	0.0335	0.0322
largest diff. peak; hole	2.13; -0.77	0.63; -0.37	1.22; -0.85	0.97; -0.96	0.78; -1.10
refined formula	$\text{Ca}_{3.23(1)}\text{Gd}_{0.77}\text{Bi}_3$	$\text{Ca}_{3.35(1)}\text{Tb}_{0.65}\text{Bi}_3$	$\text{Ca}_{3.33(1)}\text{Dy}_{0.67}\text{Bi}_3$	$\text{Ca}_{3.38(1)}\text{Ho}_{0.62}\text{Bi}_3$	$\text{Ca}_{3.27(1)}\text{Er}_{0.73}\text{Bi}_3$
f.w.	877.19	864.80	869.28	865.01	879.78
$a/\text{\AA}$	9.5782(5)	9.5706(19)	9.5538(15)	9.5590(9)	9.5596(7)
$V/\text{\AA}^3$	878.72(14)	876.6(5)	872.0(4)	873.4(4)	873.61(11)
$\rho_{\text{cal}}/\text{g cm}^{-3}$	6.63	6.55	6.62	6.58	6.69
$\mu/\text{cm}^{-1}$	674.1	671.1	679.0	677.3	689.2
$R_1$ ( $I \geq 2\sigma$ ) <sup>a</sup>	0.0205	0.0285	0.0208	0.0142	0.0290
$wR_2$ ( $I \geq 2\sigma$ ) <sup>a</sup>	0.0387	0.0567	0.0281	0.0300	0.0549
$R_1$ (all data) <sup>a</sup>	0.0215	0.0327	0.0240	0.0152	0.0340
$wR_2$ (all data) <sup>a</sup>	0.0391	0.0580	0.0288	0.0303	0.0563
largest diff. peak; hole	0.92; -0.64	1.38; -2.38	0.69; -0.87	0.69; -0.83	1.28; -1.80
refined formula	$\text{Ca}_{3.25(1)}\text{Tm}_{0.75}\text{Bi}_3$	$\text{Ca}_{3.47(1)}\text{Lu}_{0.53}\text{Bi}_3$	$\text{Ca}_{3.29(1)}\text{Y}_{0.71}\text{Bi}_3$		
f.w.	883.58	858.75	821.93		
$a/\text{\AA}$	9.5378(18)	9.555(2)	9.573(2)		
$V/\text{\AA}^3$	867.7(5)	872.5(6)	877.2(6)		
$\rho_{\text{cal}}/\text{g cm}^{-3}$	6.76	6.54	6.22		
$\mu/\text{cm}^{-1}$	700.6	682.3	664.8		
$R_1$ ( $I \geq 2\sigma$ ) <sup>a</sup>	0.0242	0.0251	0.0211		
$wR_2$ ( $I \geq 2\sigma$ ) <sup>a</sup>	0.0512	0.0479	0.0361		
$R_1$ (all data) <sup>a</sup>	0.0259	0.0274	0.0240		
$wR_2$ (all data) <sup>a</sup>	0.0517	0.0488	0.0369		
largest diff. peak; hole	0.40; -0.35	0.93; -0.91	0.99; -0.72		

<sup>a</sup>  $R_1 = \sum ||F_o| - |F_c|| / \sum |F_o|$ ;  $wR_2 = [\sum [w(F_o^2 - F_c^2)^2] / \sum [w(F_o^2)^2]]^{1/2}$ , where  $w = 1 / [\sigma^2 F_o^2 + (AP)^2 + (BP)]$ , and  $P = (F_o^2 + 2F_c^2) / 3$ ;  $A, B$  are the respective weight coefficients (please see CIF; the files have been deposited with CCDC and have been assigned deposition numbers 2132681–2132694).

### Thermopower and electrical resistivity measurements

Seebeck coefficient measurements were carried out using the integral method, and a constantan wire used as a reference on an SB-100 module MMR Tech. instrument. Appropriate geometry of the sample was mounted on the platform using a high-purity silver conductive paint and interfaced with the probe using the same silver conductive paint. Data were collected for temperatures between 300 and 600 K under high vacuum, with the sample exposed to a limited amount of air throughout the whole process.

Electrical resistivity was measured within the temperature window of 300–400 K by using a H-50 module sourced from MMR Tech. Measurements were made through the four-probe

Van der Pauw method on samples utilizing four platinum wires and high-purity silver paint to make contacts. The same temperature variable chamber was used, and an inert environment was maintained throughout the experiment through a vacuum.

### Thermal analysis

Thermogravimetric/differential scanning calorimetry (TG/DSC) experiments were conducted on selected samples using a TA Instruments SDT Q600. Analysis was conducted on samples of  $\text{Ca}_3\text{LaBi}_3$ ,  $\text{Ca}_3\text{CeBi}_3$ ,  $\text{Ca}_3\text{PrBi}_3$ ,  $\text{Ca}_3\text{LaBi}_{1.5}\text{Sb}_{1.5}$ , and  $\text{Ca}_3\text{CeBi}_{1.5}\text{Sb}_{1.5}$  with ca. 10–20 mg, which was loaded into a high purity alumina pan for analysis. Following a brief equilibration period

at 373 K, the sample was heated to 1273 K at the rate of 200 K h<sup>-1</sup>. The sample was then cooled to room temperature at the same ramp rate. An inert atmosphere was maintained by a constant flow (100 mL/min) of high-purity argon (Grade 5.0) gas.

### Electronic structure calculations

Electronic structure calculations were performed on Ca<sub>3</sub>REBi<sub>3</sub> (RE = Y, La) by utilizing the Tight-Binding Linear Muffin-Tin Orbital (TB-LMTO)-Atomic Sphere Approximation (ASA) code<sup>26</sup> implemented within the Density Functional Theory (DFT) framework. The von Barth-Hedin implementation of the local density approximation (LDA) functional was used while the tetrahedron method<sup>27</sup> was utilized for *k*-space integrations with Brillouin zone samplings of 10×10×10 *k*-point grids for both phases. For the calculations, an introduction of empty spheres was necessary to satisfy the ASA condition. The basis set taken for the calculations include the following orbitals: 4s, [4p], 3d, for Ca, 5s, [5p], 4d, [4f] for Y, 6s, [6p], 5d, 4f for La, and 6s, 6p, [6d], [5f] for Bi. The downfolded orbitals are shown in brackets and are treated with the Löwdin technique. Chemical bonding analyses were carried out based on calculations of the energy contributions of all the filled electronic states for selected pairs of atoms based on the Crystal Orbital Hamilton Population (COHP) method<sup>28</sup> available within the LMTO-ASA code.

## Results and discussions

### Synthesis and thermal stability

Here we provide additional details to the experimental section regarding the synthesis and thermal stability of the reported phases. We note that in the previous report on Ca<sub>3</sub>RESb<sub>3</sub>,<sup>16</sup> it was disclosed that synthesizing sizeable single crystals of the antimonide phases was challenging due to the exceptionally high stability of the Ca<sub>11</sub>Sb<sub>10</sub> phase. Similar problems were encountered for Ca<sub>3</sub>REBi<sub>3</sub> too. With a ratio Ca:Bi ≈ 1:1 in both Ca<sub>3</sub>REBi<sub>3</sub> and Ca<sub>11</sub>Bi<sub>10</sub>, the closeness in the compositions necessitated modifications to the reactions towards promoting the yield of the desired phase and improving on the sizes of the crystals. After several attempts, we finally arrived at an improved reaction condition utilizing a slight increase of the Bi content such that the Ca:Bi ratio of 3:3.2 achieves the task of suppressing the yield of the very stable Ca<sub>11</sub>Bi<sub>10</sub> phase. The products of these reactions are large single crystals of millimeter sizes that can be utilized for transport properties studies. It is however, important to also note that large crystals were only recovered for phases containing the light rare-earth elements. In contrast, reactions with the heavy rare-earth elements from Gd–Lu mainly produce small crystals—these observations mirror those previously reported for the Ca<sub>3</sub>RESb<sub>3</sub> phases.<sup>16</sup> Considering these findings, it is plausible to reason that the atomic sizes of the rare-earth metals play a crucial role in crystallizing Ca<sub>3</sub>REBi<sub>3</sub>.

In the synthesis of Ca<sub>3</sub>REBi<sub>3-δ</sub>Sb<sub>δ</sub> (δ ≈ 1.5), various flux synthesis approaches were carried out as follows: i) the

starting elements Ca:RE:Bi:Sb were weighed in the 3:1:20:1.5 ratio, with the large excess of Bi intended as a self-flux. Standard alumina crucibles were used. ii) The crucibles with the elemental mixtures were sealed inside fused silica ampoules and were transferred into muffle furnaces. iii) There, they were heated to 1323 K at the rate of 100 K h<sup>-1</sup>, and homogenized at this temperature for 48 h. The reaction was then slowly cooled to 873 K at the rate of 3 K h<sup>-1</sup> after which the fused silica tubes were quickly removed from the furnace, flipped, and spun in a centrifuge at high speed to remove excess molten Bi. iv) The main products of these reactions were mixtures of several binary phases, which include the “11:10” and “1:1”. Another attempt with the starting elements Ca:RE:Bi:Sb:Pb weighed in the 3:1:1.5:1.5:20 ratio did not yield the desired phase either.

Due to the inability to achieve the single crystal growth via flux synthesis, we therefore turned to the traditional solid-state synthesis approach by direct reaction which was also utilized for the reported Ca<sub>3</sub>RESb<sub>3</sub>,<sup>16</sup> RE<sub>4</sub>Sb<sub>3</sub><sup>15</sup> and Yb<sub>4-x</sub>RE<sub>x</sub>Sb<sub>3</sub><sup>14,15</sup> phases. The procedures are typical of what was reported for Ca<sub>3</sub>RESb<sub>3</sub> and are as follows: Stoichiometric amounts of the starting elements were loaded in a Nb-tube inside a glove box followed by sealing it under argon gas atmosphere. The Nb-tube was then transferred into a silica tube and sealed under a high vacuum. The sealed ampoule was loaded into a tube furnace and heated at the rate of 100 K h<sup>-1</sup> to 1298 K. At this temperature, the reaction proceeded over 72 h. Within this period of homogenization, the sample was periodically being rotated via the long tube attached to the ampoule to promote further homogenization. At the end of this period, the ampoule was removed and quenched in cold water. This method is known for the synthesis of high-temperature phases and modifications. The ampoule was opened, and the Nb-tube transferred back to the glovebox where it was opened. Subsequently, the products were finely grounded and reintroduced into another Nb-tube and annealed for 10 more days. The phase identification of the product of this reaction revealed the Ca<sub>3</sub>REBi<sub>3</sub> as a major phase with minor traces of binary RESb/Bi<sup>29–32</sup> phases, as revealed by EDX analysis and PXRD data in Figure 1 and 2, respectively.

The thermal stability of the Ca<sub>3</sub>REBi<sub>3</sub> (RE = La–Nd) and Ca<sub>3</sub>REBi<sub>1.5</sub>Sb<sub>1.5</sub> (RE = La, Ce) phases were investigated. The results of the TG/DSC analyses are presented in Figures 4 and S1. There are no observable thermal events up to 1273 K, which together with the flat nature of the thermogravimetric signal argues in support of the thermal stability of these phases up to a temperature of at least 1273 K. This reveals the stability of these phases up to a temperature of 1273 K. It is noted that similar high-temperature stability was reported for Ca<sub>3</sub>RESb<sub>3</sub> phases and therefore indicates the general high-temperature stability of these phases, which is beneficial for high-temperature thermoelectric generators.

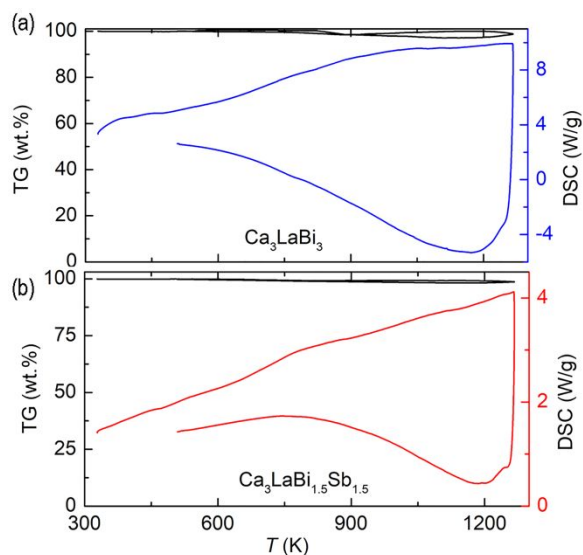


**Figure 4.** Plots from the TG/DSC analysis for  $\text{Ca}_3\text{LaBi}_3$  (a) and  $\text{Ca}_3\text{LaBi}_{1.5}\text{Sb}_{1.5}$  (b), respectively. The weights (wt. %) are represented by black line while the heat flow (W/g) data are represented by blue and red lines, respectively.

### Crystal structure

The synthesized and characterized  $\text{Ca}_3\text{REBi}_3$  and  $\text{Ca}_3\text{REBi}_{1.5}\text{Sb}_{1.5}$  phases that are presented here are analogs to the recently reported antimonides  $\text{Ca}_3\text{RESb}_3$ ,<sup>16</sup> all crystallizing in the *anti*- $\text{Th}_3\text{P}_4$  structure type with the noncentrosymmetric space group  $I\bar{4}3d$ , no. 220,  $Z = 4$ <sup>34</sup>.

The *anti*- $\text{Th}_3\text{P}_4$  structure has been extensively discussed in literatures<sup>19</sup> and features only two unique crystallographic sites (16c and 12a) and only one refineable position, as shown in Table 2 and Tables S1–S13. The 16c site is shared between the Ca and RE atoms in approximately 3 to 1 ratio, with slight deviations from the idealized “3-1-3” compositions as observed from the refined single-crystal X-ray diffraction data shown in Table 1; the EDS analyses (see Figure 1) independently confirm the refined compositions. In  $\text{Ca}_3\text{REBi}_3$ , the Bi atoms fully occupy the 12a site while this site is equally shared between Bi and Sb atoms in a 50:50 ratio in

$\text{Ca}_3\text{REBi}_{1.5}\text{Sb}_{1.5}$ . It should be noted that although four phases of the  $\text{Ca}_3\text{REBi}_{1.5}\text{Sb}_{1.5}$  compositions, namely  $\text{Ca}_3\text{LaBi}_{1.5}\text{Sb}_{1.5}$ ,  $\text{Ca}_3\text{HoBi}_{1.5}\text{Sb}_{1.5}$ ,  $\text{Ca}_3\text{ErBi}_{1.5}\text{Sb}_{1.5}$ , and  $\text{Ca}_3\text{LuBi}_{1.5}\text{Sb}_{1.5}$  were synthesized, crystallographic data for the  $\text{Ca}_3\text{HoBi}_{1.5}\text{Sb}_{1.5}$  sample only are available at this time (Table S13), affirming the structural model.

**Table 2.** Fractional Atomic Coordinates and Equivalent Isotropic Displacement Parameters ( $\text{\AA}^2$ ) for  $\text{Ca}_{3.29(1)}\text{La}_{0.71}\text{Bi}_3$ .  $U_{eq}$  is defined as 1/3 of the trace of the orthogonalized  $U_{ij}$  tensor.

atom	site	x	y	z	$U_{eq}$
Ca1/La <sup>a</sup>	16c	0.07200(2)	x	x	0.011(1)
Bi	12a	3/8	0	1/4	0.0087(4)

<sup>a</sup> Atomic occupancies according to refinement: Ca1/La1 = 0.823(13)Ca + 0.177(13)La.

A schematic representation of the crystal structure of  $\text{Ca}_3\text{LaBi}_3$  is shown in Figure 5, where the muddled arrangements of the constituent atoms is emphasized. It can be succinctly described as buckled  $[\text{Bi}_6]$  octahedra, centered by Ca/RE atoms, which are all face-shared. The Bi atoms are coordinated by eight Ca/La atoms and form two interpenetrating tetrahedra arranged into bis-disphenoid polyhedron. The refined distances are presented in Table 3. There are no Bi–Bi bonds and the two kinds of Ca/RE–Bi contacts have values of 3.19–3.23  $\text{\AA}$  and 3.42–3.46  $\text{\AA}$ , respectively. All are systematically longer than the reported distances of 3.12–3.18  $\text{\AA}$  and 3.35–3.43  $\text{\AA}$  in  $\text{Ca}_3\text{RESb}_3$ .<sup>16</sup> The distances in the bismuthides are related to the much larger covalent radius of Bi as compared to that of Sb<sup>35</sup>. Aside the much longer bond lengths observed for the bismuthides phases, the general trends, bond angles and nature of the atomic bonds are comparable to those of the isostructural antimonides. In any case, the variations of the RE compositions in the various phases will undoubtedly play a crucial role in their transport and magnetic properties. We provide further discussions on the transport properties of these materials in the Transport properties section (*vide infra*).

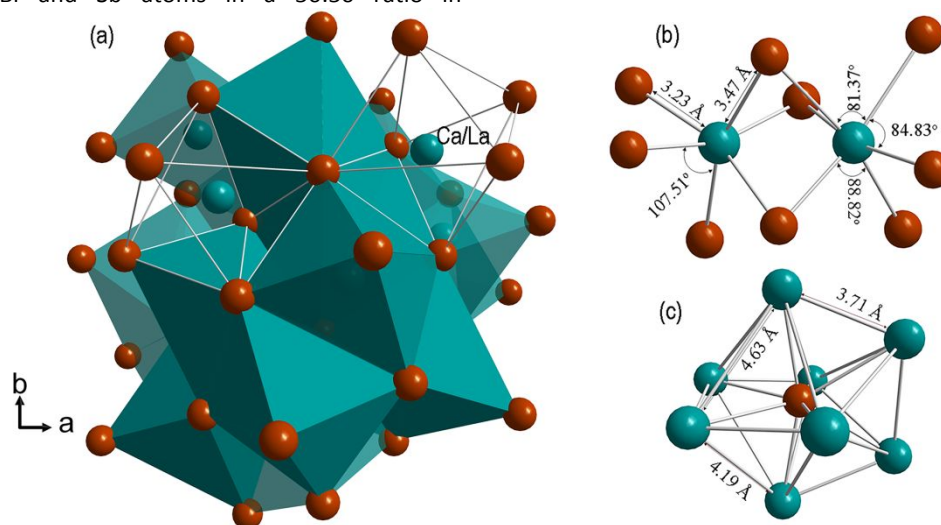


**Figure 5.** (a) Schematic representation of the crystal structure of  $\text{Ca}_3\text{LaBi}_3$ . Ca/La atoms are shown in teal, Bi atoms are in red-brown. (b) and (c) Schematic representations of the Ca/La and Bi coordination polyhedra, respectively.

**Table 3.** Ca/RE–Bi distances (Å) for  $\text{Ca}_3\text{REBi}_3$  (RE = Y, La–Nd, Sm, Gd–Tm, Lu).

Atom pair	Distances				
	$\text{Ca}_{3.29(1)}\text{La}_{0.71}\text{Bi}_3$	$\text{Ca}_{3.33(1)}\text{Ce}_{0.67}\text{Sb}_3$	$\text{Ca}_{3.35(1)}\text{Pr}_{0.66}\text{Bi}_3$	$\text{Ca}_{3.33(1)}\text{Nd}_{0.67}\text{Bi}_3$	$\text{Ca}_{3.23(1)}\text{Sm}_{0.77}\text{Bi}_3$
Ca/RE–Bi	$3.468(2) \times 3$	$3.458(1) \times 3$	$3.451(1) \times 3$	$3.449(2) \times 3$	$3.441(1) \times 3$
	$3.230(2) \times 3$	$3.222(1) \times 3$	$3.217(1) \times 3$	$3.210(1) \times 3$	$3.203(1) \times 3$
Ca/RE–Bi	$\text{Ca}_{3.23(1)}\text{Gd}_{0.77}\text{Bi}_3$	$\text{Tb}_{3.35(1)}\text{Tb}_{0.65}\text{Bi}_3$	$\text{Ca}_{3.33(1)}\text{Dy}_{0.67}\text{Bi}_3$	$\text{Ca}_{3.38(1)}\text{Ho}_{0.62}\text{Bi}_3$	$\text{Ca}_{3.27(1)}\text{Er}_{0.73}\text{Bi}_3$
	$3.433(1) \times 3$	$3.425(1) \times 3$	$3.422(1) \times 3$	$3.423(1) \times 3$	$3.428(4) \times 3$
Ca/RE–Bi	$3.203(1) \times 3$	$3.198(1) \times 3$	$3.197(1) \times 3$	$3.1994(9) \times 3$	$3.205(2) \times 3$
	$\text{Ca}_{3.25(1)}\text{Tm}_{0.75}\text{Bi}_3$	$\text{Ca}_{3.47(1)}\text{Lu}_{0.53}\text{Bi}_3$	$\text{Ca}_{3.29(1)}\text{Y}_{0.71}\text{Bi}_3$		
Ca/RE–Bi	$3.416(2) \times 3$	$3.415(2) \times 3$	$3.425(2) \times 3$		
	$3.192(1) \times 3$	$3.204(2) \times 3$	$3.207(2) \times 3$		

The structures of  $\text{Ca}_3\text{REBi}_3$  and  $\text{Ca}_3\text{REBi}_{1.5}\text{Sb}_{1.5}$  inherently harbor complex structural disorder, which is beneficial for thermoelectric applications and can be tuned via various mechanisms for substitution. As shown in the electronic calculation section (*vide infra*), the  $\text{Ca}_4\text{Bi}_3$  phase is essentially a metallic material owing to the imbalanced electron count, which can be expressed as  $(\text{Ca}^{2+})_4(\text{Bi}^{3-})_3$ . Hence the “missing”  $e^-$  goes a long way to dictate the nature of the transport properties in this material. A similar scenario plays out in the  $\text{RE}_4\text{Bi}_3$  phases too, where the electron partitioning can be expressed as  $(\text{RE}^{3+})_4(\text{Bi}^{3-})_3$ . Therefore, an aliovalent substitution of some of the  $\text{Ca}^{2+}$  ions in  $\text{Ca}_4\text{Bi}_3$  would provide for a charge-balanced system in conformity with the Zintl-Klemm formalism. Following such materials design rationale, the  $\text{Ca}_3\text{REBi}_3$  single crystals were grown. It is noted that the idea is essentially the same for the  $\text{Ca}_3\text{REBi}_{1.5}\text{Sb}_{1.5}$  phases as Sb and Bi have the same valence state, in which case one can represent the charges as  $(\text{Ca}^{2+})_3\text{RE}^{3+}(\text{Bi}^{3-})_{1.5}(\text{Sb}^{3-})_{1.5}$ . Thus, all the elements can be said to achieve a closed-shell electronic configuration. Although in the strictest sense, it is impossible to get a fully balanced electron count, considering the disorder and the slight variations in the elemental compositions of Ca and RE as compared to the ideal 3:1 ratio.

We return to discuss the nature of the unit cell volume variation across the lanthanide series as shown in Figure 3. The typical lanthanide contraction can be observed in the whole series while a slight deviation is observed for the members of the late lanthanides, such as Tm- and Lu-bearing samples. It is noted that in the reported  $\text{Ca}_3\text{RESb}_3$ <sup>16</sup>, the lanthanide contraction was followed by all the phases. The observed deviation here is associated with the refined compositions. In Lu-sample for example, the refined Lu composition is only about 2/3 of what it is in others, and since  $\text{Lu}^{3+}$  is much smaller than  $\text{Ca}^{2+}$ , this manifests in a relatively large unit cell volume. We also did carry out several single crystal measurements on some of these phases to ensure that the observed results are

consistent across various crystals from different batches and not associated with instrumental or other experimental errors.

### Electronic properties

The electronic band structures of the nonmagnetic  $\text{Ca}_3\text{YBi}_3$  and  $\text{Ca}_3\text{LaBi}_3$  phases are presented in Figures 6 and 7, respectively. The electronic structure calculations were carried out by first constructing a superstructure with an attendant effect of symmetry lowering similar to the treatment for  $\text{Ca}_3\text{RESb}_3$ <sup>16</sup>. The superstructure thus results in an orthorhombic symmetry (space group  $P2_12_12_1$ , no. 19), where the 16c site splits into four unique 4a sites with Ca and RE atoms occupying three and one sites, respectively, in accordance with the refined stoichiometric composition  $\text{Ca}_3\text{REBi}_3$  (RE = Y, La).

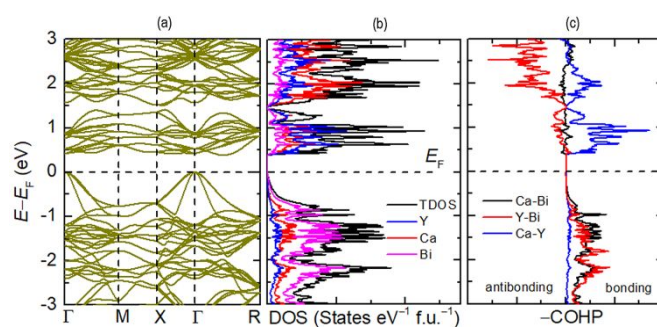


**Figure 6.** (a) Plots of the electronic band structure, (b) electronic density of states, and (c) calculated COHP curves for Ca–Bi, Y–Bi, and Ca–Y interactions for  $\text{Ca}_3\text{YBi}_3$ . COHP are showing the bonding and antibonding states as indicated. The Fermi energy is set as a reference point at 0 eV.

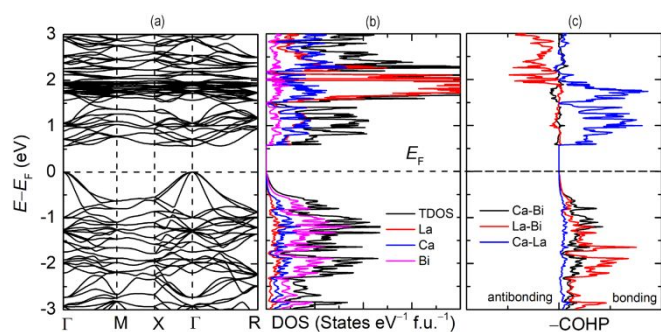


**Figure 7.** (a) Plots of the electronic band structure, (b) electronic density of states, and (c) calculated COHP curves for Ca–Bi, La–Bi, and Ca–La interactions for  $\text{Ca}_3\text{LaBi}_3$ . COHP are showing the bonding and antibonding states as indicated. The Fermi energy is set as a reference point at 0 eV.

Figure 6 (a) shows the electronic band structure of  $\text{Ca}_3\text{YBi}_3$  in the energy window of  $-3$  to  $3$  eV. The band structure features an indirect bandgap opening at the Fermi level wherein the valence band maximum (VBMA) and the conduction band minimum (CBMi) lie along the  $\Gamma$  point and  $\Lambda$  line, respectively. The estimation of the magnitude of the bandgap observed here is  $E_g = 0.38$  eV, which is indicative of a narrow bandgap. A similar observation can be made for  $\text{Ca}_3\text{LaBi}_3$  (Figure 7 a), which also possesses an indirect bandgap,  $E_g = 0.57$  eV. The bandgap calculated for these phases are within the same order of magnitude and are comparable to the reported values of  $E_g = 0.77$  and  $0.53$  eV in  $\text{Ca}_3\text{LaSb}_3$  and  $\text{Ca}_3\text{LuSb}_3$ , respectively. The higher  $E_g$  value for  $\text{Ca}_3\text{LaSb}_3$  in comparison to  $\text{Ca}_3\text{LaBi}_3$  may be attributed to the metallic character of Bi in which the replacement of Sb atoms for Bi leads to the narrowing of the bandgap. The attendant effect of such narrowing of the bandgap would be the enhancement of the electrical conductivity, albeit the Seebeck coefficient is likely to be compromised since these two thermoelectric properties are discordant in their relationship with the carrier concentration  $n$ .

From the electronic structure calculation of  $\text{Ca}_4\text{Bi}_3$  presented in Figure S2 (calculated based on the actual cubic structure since there was no need for the lowered symmetry in this case), the band structure is clearly different from that of  $\text{Ca}_3\text{YBi}_3$  and  $\text{Ca}_3\text{LaBi}_3$  and evolves in a metallic manner where the Fermi level resides within the valence band. The main reason for such difference is the imbalance in the electron count in  $\text{Ca}_4\text{Bi}_3$  as compared to those of the optimized structure  $\text{Ca}_3\text{REBi}_3$  with balanced electron count. Hence, the materials design in the title compounds achieves the aliovalent substitution of one  $\text{Ca}^{2+}$  for  $\text{RE}^{3+}$  to chemically drive the system from a metallic to a narrow bandgap semiconducting state.

Figures 6 (b) and 7 (b) show the total and partial density of states (DOS) for  $\text{Ca}_3\text{YBi}_3$  and  $\text{Ca}_3\text{LaBi}_3$ , respectively, and are reflective of the energy bandgap opening observed in the band structure calculations. In  $\text{Ca}_3\text{YBi}_3$ , the total density of states (TDOS) reveals that within the valence band, contributions from the Bi- $p$  orbital are significant followed by that of Ca- $d$ , while the Y- $d$  contributes the least. Similar observations are also noticeable in  $\text{Ca}_3\text{LaBi}_3$  where contributions to TDOS are from Bi- $p$ , Ca- $d$ , and La- $p$ , in their decreasing order. In the

conduction band however, the DOS of  $\text{Ca}_3\text{YBi}_3$  indicates a dominant contribution by Y orbitals followed by those of Ca within the energy range of ca.  $0.38$  to  $1.07$  eV, while further at high energy (above  $\sim 1.5$  eV), the contributions by Y and Ca orbitals are reversed with the Ca orbitals contributions being dominant. In the case of  $\text{Ca}_3\text{LaBi}_3$ , both the Ca and La orbitals contribute to the TDOS over the energy window of ca.  $0.57$  to  $1.5$  eV. The energy window of ca.  $1.5$  to  $2.3$  eV is mainly dominated by the La- $f$  orbital, which manifests as a spike in this region before lagging slightly behind the contributions from Ca orbitals above about  $2.5$  eV. For the other lanthanides, the  $4f$  orbitals will be partially filled and  $f$ -originated states are expected to appear on both sides of the Fermi level. This feature can potentially give rise to sharply increased DOS in an energy window that might be hugely beneficial for an increased Seebeck coefficient.

Additional insights into the nature of the bonding can be gained through their Crystal Orbital Hamilton Population (COHP) curves. The COHP curves are presented in Figures 6 (c) and 7 (c), for  $\text{Ca}_3\text{YBi}_3$  and  $\text{Ca}_3\text{LaBi}_3$ , respectively. They both feature optimized interactions as deduced from the absence of bonding and antibonding levels across their respective Fermi levels. Furthermore, the two curves are qualitatively similar with the Y–Bi and La–Bi showing antibonding character in the conduction band above the respective energy gaps. In the valence band however, all the interactions are fully bonding for the two phases presented. The integrated COHP (–ICOHP) for Ca–Bi, Ca–Y, and Y–Bi heteroatomic contacts in  $\text{Ca}_3\text{YBi}_3$  are  $0.6953$ ,  $0.1189$ , and  $0.7115$ , respectively. In  $\text{Ca}_3\text{LaBi}_3$ , the respective values for Ca–Bi, Ca–La and La–Bi are  $0.5690$ ,  $0.1489$  and  $0.7188$ . These observations here are indicative of partially covalent bonding character.

### Transport properties

For the transport properties measurements on the  $\text{Ca}_3\text{REBi}_3$  phases, suitable single crystals were selected and carefully etched (mechanically) to remove possible Pb or Bi residue on their surface. Then, leads were attached with silver paste. Figure 8 (a) presents the temperature dependence of the electrical resistivity  $\rho(T)$  of  $\text{Ca}_3\text{LaBi}_3$ ,  $\text{Ca}_3\text{CeBi}_3$ ,  $\text{Ca}_3\text{PrBi}_3$ ,  $\text{Ca}_3\text{NdBi}_3$ , and  $\text{Ca}_3\text{SmBi}_3$  in the temperature range of  $300$  to  $460$  K.  $\rho(T)$  for the five compounds evolve in a metallic manner and feature a relatively low magnitude within the temperature range studied. The  $\rho(T)$  of  $\text{Ca}_3\text{LaSb}_3$  and  $\text{Ca}_3\text{CeSb}_3$  are observed to be similar and comparable as both attain values of ca.  $0.9$  m $\Omega$ .cm and  $1.4$  m $\Omega$ .cm at  $300$  and  $460$  K, respectively. Such temperature variation in the magnitude of  $\rho(T)$  in both compounds indicates only an increase by a factor of about  $1.5$  and hence, a weak temperature dependence of  $\rho(T)$  within this temperature range. Such observation of weak temperature dependence and a relatively low magnitude of  $\rho(T)$  may also be a definitive feature of these compounds at elevated temperature, in which case would yield a significantly high electrical conductivity  $\sigma(T)$ . The situation for  $\text{Ca}_3\text{PrBi}_3$ ,  $\text{Ca}_3\text{NdBi}_3$ , and  $\text{Ca}_3\text{SmBi}_3$  samples is similar, although  $\text{Ca}_3\text{NdBi}_3$  appears to have the highest magnitude of  $\rho(T)$  out of the five

compounds with magnitudes of 2.9 m $\Omega$ .cm and 4.0 m $\Omega$ .cm at 300 and 460 K, respectively. While  $\rho(T)$  is metallic in nature, the electronic structure of  $\text{Ca}_3\text{LaSb}_3$  shown in Figure 8 reveals a semiconducting character with an indirect bandgap  $E_g = 0.57$  eV. Such a behavior is typical of the heavily doped semiconductors, where the system is driven to a degenerate semiconducting state<sup>36–39</sup>. It is also likely that the observed behavior has its origin in the deviation from the 3:1 stoichiometric ratios of Ca and RE atoms in these compounds as shown in Table 1. While the electrical transports of these compounds have only been investigated within the 300–460 K temperature window, measurements at much higher temperatures would be invaluable to confirm the earlier proposal of a significantly high  $\sigma(T)$  in these compounds.

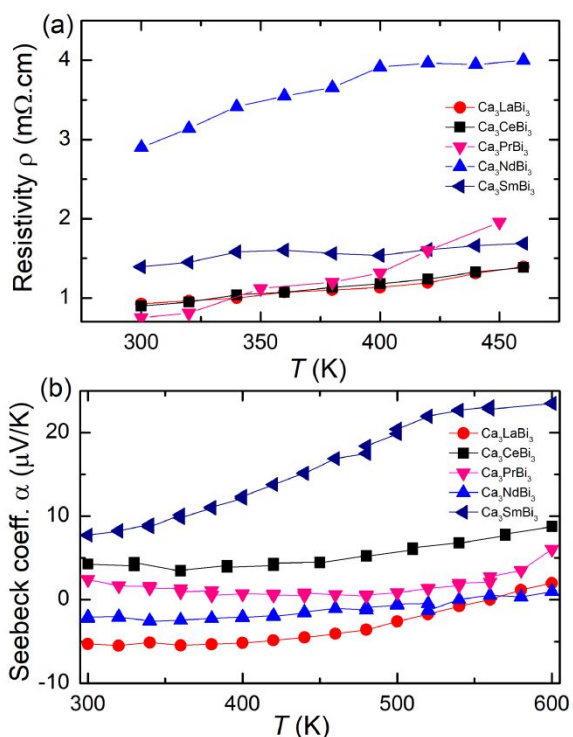


**Figure 8.** (a) Plot of temperature dependence of electrical resistivity  $\rho(T)$  and (b) Temperature dependence of Seebeck coefficient  $\alpha(T)$  of  $\text{Ca}_3\text{REBi}_3$  (RE = La, Ce, Pr, Nd, Sm) single crystals.

The temperature dependence of the Seebeck coefficient  $\alpha(T)$  of  $\text{Ca}_3\text{LaBi}_3$ ,  $\text{Ca}_3\text{CeBi}_3$ ,  $\text{Ca}_3\text{PrBi}_3$ ,  $\text{Ca}_3\text{NdBi}_3$ , and  $\text{Ca}_3\text{SmBi}_3$  measured in the temperature range of 300–600 K are presented in Figure 8 (b). Within the said temperature range,  $\alpha(T)$  of these five compounds is relatively low.  $\text{Ca}_3\text{LaBi}_3$  and  $\text{Ca}_3\text{NdBi}_3$  attain values of  $-5.3$   $\mu\text{V/K}$  and  $-2.3$   $\mu\text{V/K}$ , respectively, at room temperature, which suggests dominant electron charge carriers. However, upon further heating, a

crossover from negative to positive values is observed in both phases near 540 K, thus achieving values of 2.0  $\mu\text{V/K}$  and 1.9  $\mu\text{V/K}$  for  $\text{Ca}_3\text{LaBi}_3$  and  $\text{Ca}_3\text{NdBi}_3$ , respectively. It is noted that similar crossovers were observed in  $\text{RE}_4\text{Sb}_3$  and  $\text{Yb}_3\text{RESb}_3$ <sup>15</sup>. The Seebeck coefficients of the Ce-, Pr- and Sm-based phases are positive throughout the investigated temperature range, which indicates a  $p$ -type material with dominant hole carriers. The magnitude of  $\alpha(T)$  for  $\text{Ca}_3\text{CeBi}_3$  varies from 4.3  $\mu\text{V/K}$  (300 K) to 8.8  $\mu\text{V/K}$  (600 K), for  $\text{Ca}_3\text{PrBi}_3$  it varies from 2.4  $\mu\text{V/K}$  (300 K) to 6.1  $\mu\text{V/K}$  (600 K) and from 7.7  $\mu\text{V/K}$  (300 K) to 23.5  $\mu\text{V/K}$  (600 K) in  $\text{Ca}_3\text{SmBi}_3$ . Within this temperature range,  $\alpha(T)$  of  $\text{Ca}_3\text{SmBi}_3$  shows the highest increase (by a factor of about 3) as well as the highest magnitude at 600 K. Although the attainment of a higher magnitude of the Seebeck coefficients might be plausible at a much higher temperature, it is noted that within the same temperature range, the  $\text{Ca}_3\text{RESb}_3$  phases feature significantly higher values of  $\alpha(T)$ . It can therefore be speculated that while the replacement of Sb with Bi, which is a much heavier element, can bring about an enhanced phonon scattering, as well as generate a strong spin-orbit coupling that can trigger the emergence of topological properties of interest, the presence of Bi may lead to a lowering of the  $\alpha$ -values.

Although the thermal conductivities  $\kappa(T)$  of these materials are not immediately available, the structural complexity and disorder inherent in them is expected to bring about a significant reduction in the magnitude of  $\kappa(T)$ . In addition to the disorder introduced to the 16c atomic site, one can further introduce a significant disorder to the 12a site by substituting Bi with Sb. Such material design not only ensures to lower the magnitude of the  $\kappa(T)$ , but also can bring about a much higher  $\alpha(T)$  as compared to the values achieved in  $\text{Ca}_3\text{REBi}_3$ . Here, we provide a glimpse into such materials design. Figure 9 (a) presents a plot of  $\alpha(T)$  for  $\text{Ca}_3\text{LaBi}_{1.5}\text{Sb}_{1.5}$ ,  $\text{Ca}_3\text{HoBi}_{1.5}\text{Sb}_{1.5}$ ,  $\text{Ca}_3\text{ErBi}_{1.5}\text{Sb}_{1.5}$ , and  $\text{Ca}_3\text{LuBi}_{1.5}\text{Sb}_{1.5}$  in the temperature range of 300–600 K. The four compounds reveal  $\alpha(T)$  values that are positive within this temperature range, indicating  $p$ -type materials. The Er-based compound shows a very weak temperature dependence as well as the lowest values of ca. 4.5  $\mu\text{V/K}$  and 8.1  $\mu\text{V/K}$  at room temperature and 600 K, respectively.  $\alpha(T)$  of La-, Ho-, and Lu-based materials on the other hand reveal strong temperature dependence that continues to increase with heating.  $\text{Ca}_3\text{LaBi}_{1.5}\text{Sb}_{1.5}$ ,  $\text{Ca}_3\text{HoBi}_{1.5}\text{Sb}_{1.5}$ , and  $\text{Ca}_3\text{LuBi}_{1.5}\text{Sb}_{1.5}$  achieve values of ca. 23.8  $\mu\text{V/K}$ , 30.0  $\mu\text{V/K}$ , and 44.0  $\mu\text{V/K}$ , respectively, at room temperature. These values are significantly higher than what is observed in  $\text{Ca}_3\text{REBi}_3$  but still relatively lower than some of the  $\text{Ca}_3\text{RESb}_3$  materials in this temperature range. Here,  $\text{Ca}_3\text{LuBi}_{1.5}\text{Sb}_{1.5}$  achieves the highest value of ca. 75.2  $\mu\text{V/K}$  while  $\text{Ca}_3\text{LaBi}_{1.5}\text{Sb}_{1.5}$  and  $\text{Ca}_3\text{HoBi}_{1.5}\text{Sb}_{1.5}$  achieve close values of 51.4  $\mu\text{V/K}$  and 53.3  $\mu\text{V/K}$ , respectively, at 600 K.

## ARTICLE

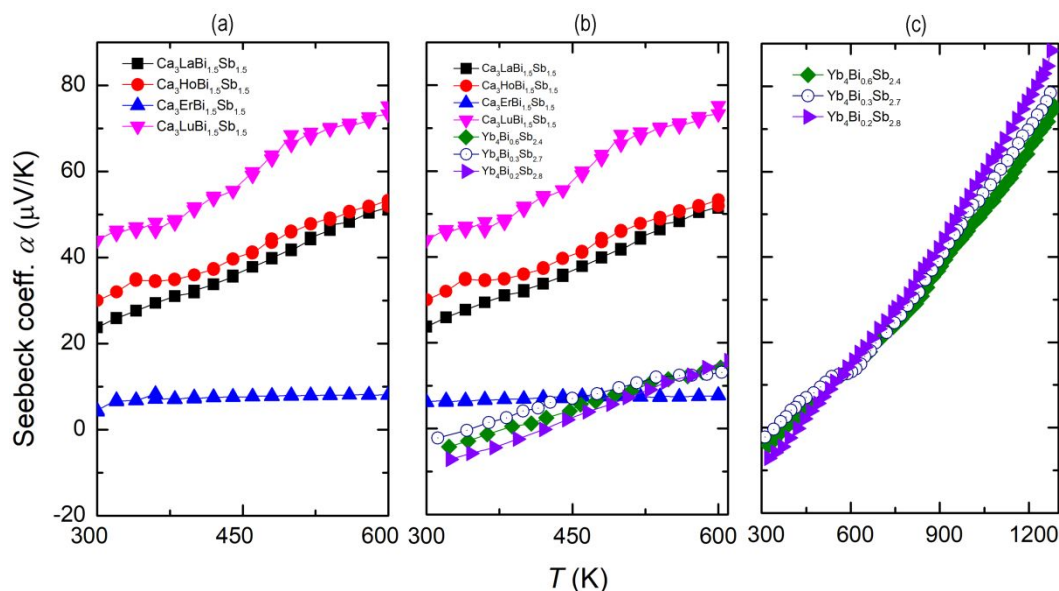


**Figure 9.** (a)  $\alpha(T)$  of  $\text{Ca}_3\text{REBi}_{1.5}\text{Sb}_{1.5}$  ( $\text{RE} = \text{La}, \text{Ho}, \text{Er}, \text{Lu}$ ) cold-pressed pellets. (b)  $\alpha(T)$  of  $\text{Ca}_3\text{REBi}_{1.5}\text{Sb}_{1.5}$  ( $\text{RE} = \text{La}, \text{Ho}, \text{Er}, \text{Lu}$ ) cold-pressed pellets together with those of reported  $\text{Yb}_4\text{Sb}_{3-6}\text{Bi}_6$  ( $0.2 \leq \delta \leq 0.6$ ) compounds.

To put the transport properties observed here in perspective, we estimated the power factor  $PF = \alpha^2/\rho$ . The estimated magnitude of  $PF$  in  $\text{Ca}_3\text{SmBi}_3$  is ca.  $0.33 \text{ W}/(\text{cm K}^2)$  near 600 K which is the highest value observed in  $\text{Ca}_3\text{REBi}_3$  within the investigated temperature range. Here, the  $PF$  of  $\text{Ca}_3\text{CeBi}_3$  and  $\text{Ca}_3\text{PrBi}_3$  are about an order of magnitude lower than that of  $\text{Ca}_3\text{SmBi}_3$ , while  $\text{Ca}_3\text{NdBi}_3$  shows the least magnitude considering its manifest relatively low  $\rho(T)$  and high  $\alpha(T)$ . Although the magnitude of  $PF$  in  $\text{Ca}_3\text{SmBi}_3$  is relatively low, it is relatively higher than those of  $\text{RE}_4\text{Sb}_3$ <sup>14,15</sup> and comparable to that of  $\text{Yb}_4\text{Bi}_{3-x}\text{Sb}_x$  around the same temperature<sup>40</sup>. Also, it is worth mentioning that the break-out advantage of these materials would lie in their thermal conductivity which is expected to be very low based on the prevalent intricate bonding and atomic disorder at play in them. This line of thought is plausible if one considers the low thermal conductivity observed in  $\text{Yb}_{4-x}\text{RE}_x\text{Sb}_3$  and  $\text{Yb}_4\text{Bi}_{3-x}\text{Sb}_x$ <sup>15,40</sup> and as such, the magnitude of thermal conductivity in  $\text{Ca}_3\text{REBi}_3$  is expected to be of comparable magnitude to the reported Yb-based phases.

In Figure 9 (b), we compare the  $\alpha$ -values of the reported phases along with those of  $\text{Yb}_4\text{Bi}_{3-6}\text{Sb}_6$  by Chamoire *et al.*<sup>40</sup> The three phases, namely  $\text{Yb}_4\text{Bi}_{0.6}\text{Sb}_{2.4}$ ,  $\text{Yb}_4\text{Bi}_{0.3}\text{Sb}_{2.7}$  and  $\text{Yb}_4\text{Bi}_{0.2}\text{Sb}_{2.8}$  have negative  $\alpha$ -value near 400 K after which the holes dominate the transport mechanism upon further heating.  $\alpha(T)$  of these materials within the temperature range

of 300–600 K presents a comparable temperature dependence and slope with those of  $\text{Ca}_3\text{LaBi}_{1.5}\text{Sb}_{1.5}$ ,  $\text{Ca}_3\text{HoBi}_{1.5}\text{Sb}_{1.5}$ , and  $\text{Ca}_3\text{LuBi}_{1.5}\text{Sb}_{1.5}$ . As earlier discussed, the  $\text{Ca}_3\text{REBi}_3$  materials feature a relatively low  $\rho(T)$  values which is beneficial for thermoelectric applications, it is not immediately clear what the nature of this physical property would be in the case of  $\text{Ca}_3\text{REBi}_{3-6}\text{Sb}_6$  ( $\text{RE} = \text{La}, \text{Ho}, \text{Er}, \text{Lu}; \delta \approx 1.5$ ). In  $\text{Yb}_4\text{Bi}_{3-6}\text{Sb}_6$ <sup>40</sup>, however, values achieved at high temperatures are relatively smaller than those of  $\text{Yb}_{4-x}\text{RE}_x\text{Sb}_3$ <sup>15</sup>.

Quantitatively, the magnitude of  $\alpha(T)$  for the  $\text{Yb}_4\text{Bi}_{3-6}\text{Sb}_6$  materials lag those of  $\text{Ca}_3\text{LaBi}_{1.5}\text{Sb}_{1.5}$ ,  $\text{Ca}_3\text{HoBi}_{1.5}\text{Sb}_{1.5}$ , and  $\text{Ca}_3\text{LuBi}_{1.5}\text{Sb}_{1.5}$  by factors of between 5–10 at 600 K. Figure 9 (c) shows  $\text{Yb}_4\text{Bi}_{3-6}\text{Sb}_6$  materials and at a much higher temperature of up to 1275 K. A close observation of these results shows that although  $\text{Yb}_4\text{Bi}_{0.2}\text{Sb}_{2.8}$  has the lowest  $\alpha(T)$  at room temperature, it invariably achieves the highest value of 88.4 K at 1275 K. It is thought that the much lower value of  $\text{Yb}_4\text{Bi}_{0.2}\text{Sb}_{2.8}$  at low temperature is connected with its strong temperature dependence which manifests in a steep slope as compared to others thereby showing significant increase above the other two materials. This notion may also be at play in the phases reported here especially considering the case of  $\text{Ca}_3\text{LaBi}_{1.5}\text{Sb}_{1.5}$ ,  $\text{Ca}_3\text{HoBi}_{1.5}\text{Sb}_{1.5}$ , and  $\text{Ca}_3\text{LuBi}_{1.5}\text{Sb}_{1.5}$ . Here, the La-based phase has the lowest value at room temperature, which achieves a much steeper slope and can bring about a much-enhanced  $\alpha(T)$  value at elevated temperature. In fact, this may

be apparent in Figure 8 (b), where the magnitude of  $\alpha(T)$  for  $\text{Ca}_3\text{LaBi}_{1.5}\text{Sb}_{1.5}$  already appears to catch up with that of  $\text{Ca}_3\text{HoBi}_{1.5}\text{Sb}_{1.5}$  near 600 K. Hence, it is expected that at a much higher temperature  $\text{Ca}_3\text{LaBi}_{1.5}\text{Sb}_{1.5}$  is likely to attain even higher value as compared to those of  $\text{Ca}_3\text{HoBi}_{1.5}\text{Sb}_{1.5}$  and  $\text{Ca}_3\text{LuBi}_{1.5}\text{Sb}_{1.5}$ . Lastly, it is also worth mentioning that the reduction in the Bi atom concentration appears to favor an enhanced  $\alpha(T)$  in the  $\text{Yb}_4\text{Bi}_{3-\delta}\text{Sb}_\delta$  phases. Therefore, a reduction in the Bi atom concentration in  $\text{Ca}_3\text{REBi}_{3-\delta}\text{Sb}_\delta$  could also be beneficial toward tuning the thermoelectric properties of these materials—after all, the end members have been shown to exist for all lanthanides, and as the preliminary data from this report indicate, it is very likely that continuous solid solutions will exist. Thus, one may envision the  $\text{Ca}_3\text{REBi}_{3-\delta}\text{Sb}_\delta$  system as a strong candidate for future optimization studies, where one might achieve both the desire to lower the thermal conductivity and improve the magnitude of  $\alpha(T)$  of the measured samples.

## Conclusions

We have reported on the synthesis, structural elucidation and some transport properties for  $\text{Ca}_3\text{REBi}_3$  ( $\text{RE} = \text{Y, La-Nd, Sm, Gd-Tm, Lu}$ ) and  $\text{Ca}_3\text{REBi}_{1.5}\text{Sb}_{1.5}$  ( $\text{RE} = \text{La, Ho, Er, Lu}$ ) Zintl phases which crystallize with the cubic *anti*- $\text{Th}_3\text{P}_4$  structure type. The introduction of the RE atoms into the crystal structure drives the respective phases to a nearly electron-balanced scenario whereby the constituent elements achieve closed-shell electronic. The observed unit cell volumes generally follow the lanthanide contraction with a slight deviation observed for the phases with very late lanthanides.  $\text{Ca}_3\text{REBi}_3$  feature a relatively low  $\rho(T)$  that evolves in a metallic manner which indicates both an enhanced electrical conductivity across the series as well as the realization of a degenerate semiconducting state. Electronic structure calculations on  $\text{Ca}_3\text{YBi}_3$  and  $\text{Ca}_3\text{LaBi}_3$  predict indirect bandgaps with  $E_g = 0.38$  eV and 0.57 eV, respectively. However, the observed magnitude of  $\alpha(T)$  which indicates p-type materials are relatively small. It is thought that although the heavy nature of Bi atoms brings about a strong spin-orbit coupling effects as well as serves the purpose of phonon scattering which is desirable, its overall metallic nature is counter intuitive to the most desired high magnitude of  $\alpha(T)$ . Regardless, the overall features are in favors of optimizing  $zT$  with proper tuning of the carrier concentration.

The  $\text{Ca}_3\text{REBi}_{1.5}\text{Sb}_{1.5}$  phases present an even more interesting scenario with an additional twist to the structure-property relationship perspective. Firstly, the modification of the crystal structure to accommodate both the Bi and Sb atoms engineered additional disorder and complexity that benefits low  $\kappa(T)$ . On the second outlook, a dramatic increase in  $\alpha(T)$  is observed for such atomic compositions and hints at the amenability of these phase to appropriate doping studies towards optimizing  $zT$ . It is noted that in  $\text{Ca}_3\text{LuBi}_{1.5}\text{Sb}_{1.5}$ , the highest  $\alpha(T)$  value of 75.2  $\mu\text{V/K}$  at 600 K is observed which likely points to the role of the  $\text{RE}^{3+}$  size on the thermoelectric transport properties.

While the magnetic properties of these phases are not immediately available, it would be of interest to know how the nature of the unit cell volumes observed interplay with the magnetic moments of the RE atoms. Also, the presence of magnetic species in these phases would likely result in a long-range magnetic ordering of the RE moments at reasonably low temperatures. Furthermore, although the focus of the present studies is not on the exploration of the topological insulator properties of these phases, it is however expected that features in these phases such as the presence of heavy atoms and the reasonably small  $E_g$  observed makes the materials prone to likely band inversion under the influence of strong spin-orbit coupling.

## Author Contributions

Michael O. Ogunbunmi: Conceptualization, Investigation, Methodology, Formal analysis, Visualization, Writing - original draft.

Sviatoslav Baranets: Conceptualization, Investigation, Formal analysis, Writing - review & editing.

Svilen Bobev: Conceptualization, Supervision, Project administration, Writing - review & editing.

## Conflicts of interest

There are no conflicts to declare.

## Acknowledgements

This work was supported by the U.S. Department of Energy, Office of Science, Basic Energy Sciences through grant DE-SC0008885.

## Notes and references

- H. Li, S.-Y. Gao, S.-F. Duan, Y.-F. Xu, K.-J. Zhu, S.-J. Tian, J.-C. Gao, W.-H. Fan, Z.-C. Rao, J.-R. Huang, J.-J. Li, D.-Y. Yan, Z.-T. Liu, W.-L. Liu, Y.-B. Huang, Y.-L. Li, Y. Liu, G.-B. Zhang, P. Zhang, T. Kondo, S. Shin, H.-C. Lei, Y.-G. Shi, W.-T. Zhang, H.-M. Weng, T. Qian and H. Ding, *Phys. Rev. X*, 2019, **9**, 041039.
- M. O. Ogunbunmi, S. Baranets, A. B. Childs and S. Bobev, *Dalton Trans.*, 2021, **50**, 9173–9184.
- S. M. Kauzlarich, S. R. Brown and G. J. Snyder, *Dalton Trans.*, 2007, 2099–2107.
- D. H. Fabini, M. Koerner and R. Seshadri, *Chem. Mater.*, 2019, **31**, 1561–1574.
- S. Azam, S. A. Khan and S. Goumri-Said, *Mater. Res. Bull.*, 2015, **70**, 847–855.
- R. Nesper, *Z. Anorg. Allg. Chem.*, 2014, **640**, 2639–2648.
- G. J. Snyder and E. S. Toberer, *Nat. Mater.*, 2008, **7**, 105–114.
- C.-C. Zhao and C. Xiao, *Rare Met.*, 2021, **40**, 752–766.
- M. O. Ogunbunmi and A. M. Strydom, *J. Phys. Condens. Matter*, 2020, **32**, 405606.
- J.-B. Vaney, S. Aminorroaya Yamini, H. Takaki, K. Kobayashi, N. Kobayashi and T. Mori, *Mater. Today Phys.*, 2019, **9**, 100090.

- 11 A. M. Goforth, P. Klavins, J. C. Fettinger and S. M. Kauzlarich, *Inorg. Chem.*, 2008, **47**, 11048–11056.
- 12 Y. Hu, C.-W. Chen, H. Cao, F. Makhmudov, J. H. Grebenkemper, M. N. Abdusalyamova, E. Morosan and S. M. Kauzlarich, *J. Am. Chem. Soc.*, 2016, **138**, 12422–12431.
- 13 N. Xu, Y. Xu and J. Zhu, *npj Quantum Mater.*, 2017, **2**, 51.
- 14 A. Chamoire, F. Gascoin, C. Estournès, T. Caillat and J.-C. Tédénac, *J. Electron. Mater.*, 2010, **39**, 1579–1582.
- 15 A. Chamoire, F. Gascoin, C. Estournès, T. Caillat and J.-C. Tédénac, *Dalton Trans.*, 2010, **39**, 1118–1123.
- 16 M. O. Ogunbunmi, S. Baranets and S. Bobev, *Chem. Mater.*, 2021, **33**, 9382–9392.
- 17 F. Holtzberg, T. R. McGuire, S. Methfessel and J. C. Suits, *J. Appl. Phys.*, 1964, **35**, 1033–1038.
- 18 R. J. Gambino, *J. Less Common Met.*, 1967, **12**, 344–352.
- 19 D. Hohnke, E. Parthé, *Acta Crystallogr.*, 1966, **21**, 435–437.
- 20 K. Deller and B. Eisenmann, *Zeitschrift für Naturforsch. B*, 1976, **31**, 29–34.
- 21 S. Baranets and S. Bobev, *J. Am. Chem. Soc.*, 2021, **143**, 65–68.
- 22 G. M. Sheldrick, *Acta Crystallogr. A*, 2015, **71**, 3–8.
- 23 G. M. Sheldrick, *Acta Crystallogr. C*, 2015, **71**, 3–8.
- 24 O.V. Dolomanov and L.J. Bourhis and R.J. Gildea and J.A.K. Howard and H. Puschmann, *J. Appl. Crystallogr.*, 2009, **42**, 339–341.
- 25 L. M. Gelato and E. Parthé, *J. Appl. Crystallogr.*, 1987, **20**, 139–143.
- 26 O. Jepsen and O.K. Andersen, The Stuttgart TB-LMTO-ASA Program, version 4.7. Max-Planck-Institut für Festkörperforschung: Stuttgart, Germany, 1999.
- 27 P. E. Blöchl, O. Jepsen and O. K. Andersen, *Phys. Rev. B*, 1994, **49**, 16223–16233.
- 28 R. Dronskowski and P. E. Blöchl, *J. Phys. Chem.*, 1993, **97**, 8617–8624.
- 29 M. N. Abdusalyamova, O. R. Burnashev and K. E. Mironov, *J. Less Common Met.*, 1984, **102**, L19–L22.
- 30 P. Fischer, W. Hälgl and F. Hulliger, *Phys. B+C*, 1985, **130**, 551–554.
- 31 H. R. Child, M. K. Wilkinson, J. W. Cable, W. C. Köhler and E. O. Wollan, *Phys. Rev.*, 1963, **131**, 922–931.
- 32 M. N. Abdusalyamova, H. S. Shokirov, and O. I. Rakhmatov, *J. Less Common Met.*, 1990, **166**, 221–227.
- 33 S. Furuse, A. Kjekshus, S. Åsen, H. Halvarson and L. Nilsson, *Acta Chem. Scand.*, 1964, **18**, 1180–1195.
- 34 M. Zumbusch, *Z. Anorg. Allg. Chem.*, 1941, **245**, 402–408.
- 35 B. Cordero, V. Gómez, A. E. Platero-Prats, M. Revés, J. Echeverría, E. Cremades, F. Barragán and S. Alvarez, *Dalton Trans.*, 2008, 2832–2838.
- 36 E. S. Toberer, S. R. Brown, T. Ikeda, S. M. Kauzlarich and G. J. Snyder, *Appl. Phys. Lett.*, 2008, **93**, 062110.
- 37 A. Ovchinnikov, J. Prakash and S. Bobev, *Dalton Trans.*, 2017, **46**, 16041–16049.
- 38 Y. Wang and S. Bobev, *Chem. Mater.*, 2018, **30**, 3518–3527.
- 39 S. R. Brown, S. M. Kauzlarich, F. Gascoin and G. J. Snyder, *Chem. Mater.*, 2006, **18**, 1873–1877.
- 40 A. Chamoire, R. Viennois, J.-C. Tédénac, M. M. Koza and F. Gascoin, *J. Electron. Mater.*, 2011, **40**, 1171–1175.